CrossMark

Laboratory evidence for particle mobilization as a mechanism for permeability enhancement via dynamic stressing

Thibault Candela [a,b,*], Emily E. Brodsky [b], Chris Marone [a], Derek Elsworth [a]

[a] Dept. Geosciences, Penn. State Univ., University Park, PA, United States
[b] Dept. Earth Sciences, UC Santa Cruz, Santa Cruz, CA, United States

ARTICLE INFO

ABSTRACT

It is well-established that seismic waves can increase the permeability in natural systems, yet the mechanism remains poorly understood. We investigate the underlying mechanics by generating well-controlled, repeatable permeability enhancement in laboratory experiments. Pore pressure oscillations, simulating dynamic stresses, were applied to intact and fractured Berea sandstone samples under confining stresses of tens of MPa. Dynamic stressing produces an immediate permeability enhancement ranging from 1 to 60%, which scales with the amplitude of the dynamic strain (7×10^{-7} to 7×10^{-6}) followed by a gradual permeability recovery. We investigated the mechanism by: (1) recording deformation of samples both before and after fracturing during the experiment, (2) varying the chemistry of the water and therefore particle mobility, (3) evaluating the dependence of permeability enhancement and recovery on dynamic stress amplitude, and (4) examining micro-scale pore textures of the rock samples before and after experiments. We find that dynamic stressing does not produce permanent deformation in our samples. Water chemistry has a pronounced effect on the sensitivity to dynamic stressing, with the magnitude of permeability enhancement and the rate of permeability recovery varying with ionic strength of the pore fluid. Permeability recovery rates generally correlate with the permeability enhancement sensitivity. Microstructural observations of our samples show clearing of clay particulates from fracture surfaces during the experiment. From these four lines of evidence, we conclude that a flow-dependent mechanism associated with mobilization of fines controls both the magnitude of the permeability enhancement and the recovery rate in our experiments. We also find that permeability sensitivity to dynamic stressing increases after fracturing, which is a process that generates abundant particulate matter in situ. Our results suggest that fluid permeability in many areas of the Earth's crust, particularly where pore fluids favor particle mobilization, should be sensitive to dynamic stressing.

1. Introduction

Earthquakes can cause changes in hydrologic properties of the Earth's crust up to thousands of kilometers from the main-shock. Transient changes in water well levels, anomalous tidal responses, mud volcanoes and geysers, and anomalous stream- and spring-discharge all occur surprisingly far from the causative earthquakes (Coble, 1965; Roeloffs, 1998; Brodsky et al., 2003; Elkhoury et al., 2006; Xue et al., 2013; Manga et al., 2003; Manga and Rowland, 2009; Manga, 2007; Manga and Wang, 2007). At such large distances the static stress changes caused by slip on the ruptured fault are very small, and only dynamic stresses, i.e. shaking, can be invoked to explain the observations. Dynamic shaking can also enhance oil recovery, which explains the long history of study on stimulation by low-amplitude stresses to enhance

fluid flow in petroleum reservoirs (Beresnev and Johnson, 1994; Nikolaevskiy et al., 1996; Kouznetsov et al., 1998; Roberts et al., 2003).

A growing body of evidence suggests that many of these hydrological responses to seismic waves are most easily explained by increases in permeability that persist after the passage of the seismic waves (Manga et al., 2003; Manga and Brodsky, 2006; Elkhoury et al., 2006; Doan et al., 2007; Elkhoury et al., 2011; Xue et al., 2013). The dynamic strains of passing seismic waves can result in large oscillations in pore pressure which in turn drive permeability changes (Brodsky et al., 2003). More speculatively, this cascade of interactions between earthquakes and water may even remotely trigger earthquakes (Brodsky et al., 2003; van der Elst et al., 2013). In this scenario, dynamic stresses increase the aquifer permeability and accelerate diffusion of pore pressure into faults, causing destabilization.

Seismically-generated permeability changes are well-documented in direct water well measurements, but the mechanism by

* Corresponding author.

which dynamic stressing, via seismic waves or otherwise, causes persistent permeability changes is unknown. Although permeability changes due to persistent changes in effective stress have long been known (e.g., Gangi, 1978), the persistent permeability increase in response to oscillatory transient forcing requires a new explanation (Manga et al., 2012). Mobilization of particles has been a leading candidate, yet there has been no direct evidence for its efficacy (Roberts, 2005; Roberts and Abdel-Fattah, 2009; Liu and Manga, 2009; Elkhoury et al., 2011). Oscillations in pore pressure resulting from the passage of seismic waves could drive a flow that dislodges fine particles clogging pore throats, which would generate dynamic permeability enhancement (Brodsky et al., 2003; Roberts, 2005; Elkhoury et al., 2011). In this case, the gradual recovery of permeability to its initial state could be related to re-clogging of pore throats via slow migration of fine particles after the dynamic stimulation. Another possibility is that the transient stresses cause micro-fracturing damage. The pore-pressure oscillations result in effective stress oscillations that could result in crack growth. Growth of micro-cracks that heal quickly could lead to persistent, but recoverable permeability changes (Liu and Manga, 2009; Manga et al., 2012). A third possibility is that poroelastic flow out of a fracture could impose a separation between the direct increase in fracture aperture and recovery processes that results in a long-term increase in fracture permeability immediately after an oscillatory perturbation (e.g., Faoro et al., 2012).

Prior laboratory experiments show that pore pressure oscillations can produce permeability increases in lithified rock that: (1) scale with amplitude of the perturbations and (2) persist long after the oscillations cease (Elkhoury et al., 2011). Here we expand on existing works and report on a systematic set of experiments to explore the evolution of permeability for intact and fractured rock for a range of water solution chemistries and flow rates. Our experimental set-up is designed to separate the three major candidate mechanisms: (i) dislodging of fines by oscillatory flow followed by the progressive re-clogging of pore throats via slow migration of fines, (ii) damage followed by micro-fracture healing, (iii) direct increase in aperture followed by poroelastic drainage resulting in prolonged fracture opening. We impose dynamic stresses via pore fluid pressure oscillations and analyze the resulting evolution of permeability. We also studied pore structure and fracture microstructure before and after sample deformation. Our experiments are qualitatively different than other studies of permeability evolution that focused on sand or glass-bead packs (Thomas and Chrysikopoulos, 2007), step-changes in fluid pressure (Faoro et al., 2012) or solid mechanical stress (Roberts, 2005; Liu and Manga, 2009).

We begin by summarizing the laboratory configuration and experiment details and then outline our study strategy of four distinct experimental tests with their mechanistic implications. Following an overview of the results to orient the reader, we carefully articulate the test predictions and then proceed with a point-by-point comparison of the data to the predictions of each mechanism. Our results indicate that particle mobility is the most likely candidate, and thus we close with an examination of the theoretical basis for coupling particle mobilization to fluid chemistry, including the possibility that dynamic permeability enhancement is most effective in regions, or times, with unusual water chemistry.

2. Experimental apparatus and set-up

The experimental apparatus consists of a pressure vessel within a biaxial load frame (Samuelson et al., 2009; Ikari et al., 2009). Rock samples are subjected to a true triaxial stress state under controlled pore fluid pressure via two applied loads and the confining pressure (Fig. 1). Each axis of triaxial loading is servo-controlled independently and all stresses, strains, fluid pressures and fluid volumes were measured continuously during experiments. Fluid permeability was measured using upstream and downstream pore-pressure intensifiers (Fig. 1).

All stresses, displacements and strains were measured with a 24-bit analog to digital converter at 10 kHz and averaged to recording rates of 1 to 100 Hz depending on the experiment stage. Vertical and horizontal load point displacements were measured with Direct-Current Displacement Transducers (DCDT) mounted on the biaxial load frame (Fig. 1). To determine elastic strain and damage across the future fracture plane, we used a Linear Variable Differential Transformer (LVDT) mounted within the pressure vessel (Fig. 1(d)). All displacements were recorded with ± 0.1 μm precision. Applied stresses were measured with strain gauge load cells, calibrated with a proving ring traceable to the National Bureau of Standards, and recorded with force resolution of ± 10 N (~ 4.4 kPa on the eventual fracture plane which has nominal dimensions of 45 mm $\times$ 50 mm, Fig. 1). Fluid pressures were measured using transducers mounted at the pressure intensifiers accurate to ± 0.007 MPa.

We used samples of Berea Sandstone, which were: (1) cut into L-shaped blocks measuring $68 \times 45 \times 50 \times 29$ mm (Fig. 1(b)), (2) presaturated with the pore fluid to be used during the experiment, (3) jacketed in a latex membrane, and (4) placed in the direct shear configuration (Fig. 1).

Experiments started with application of a small stress applied in the direction normal to the major plane of the L-shaped sample (this will be the normal stress across the future fracture plane), after which confining pressure was applied. Normal stress and confining pressures were then raised to the target values of 10–40 MPa and 5–16 MPa, respectively, (Table 1). These stresses were maintained constant via fast-acting servohydraulic controllers. The vertical ram of the biaxial load frame was used to apply stress to the top of the sample, via a displacement rate boundary condition. We explored a range of effective normal stresses from 9.5–40 MPa, depending on the applied pore pressure (Table 1).

After the triaxial stress state on a sample was established, we initialized fluid flow through the samples using de-aired, distilled water or brine (Table 1). Pore pressures were servo-controlled independently and applied via a line source at an inlet and outlet, such that flow occurred along the future fracture plane (Fig. 1). The fluid inlet and outlet consist of a narrow channel (1 mm wide 45 mm long, Fig. 1) fed by five 1.6 mm dia. holes in order to homogeneously distribute the flow along the width of the sample (Fig. 1(e)). We applied first a pore pressure Pp at the outlet and flushed the system until clear fluid (without any air bubbles) flowed from the inlet, which was open to the atmosphere. Then the inlet Pp line was connected and we applied a controlled differential pore pressure ΔPp at a given mean value (Table 1). For our suite of experiments, Pp and ΔPp were 2.75–3 MPa and 0.1–0.5 MPa, respectively (see Table 1). Pore pressures were then maintained constant except for imposed pore pressure oscillations.

In order to simulate dynamic stresses, we imposed sinusoidal oscillations in the upstream pore pressure while holding the downstream pore pressure constant (Fig. 2), following the technique of Elkhoury et al. (2011). Dynamic stresses were applied at constant total normal stress via oscillating fluid pressure at the upstream end of the sample (Fig. 1). A range of dynamic stress perturbations were tested (Table 1). We then raised the shear stress until the sample fractured (Fig. 2). For each experiment, we imposed multiple sets of pore pressure oscillations of varying amplitude (0.01–0.5 MPa) on both the intact and fractured sample. We explored the affect of Pp oscillation amplitude but kept the duration (120 s) and period (20 s) constant. The waiting time between sets of dynamic stressing varied between 5 and 45 min (Fig. 2).
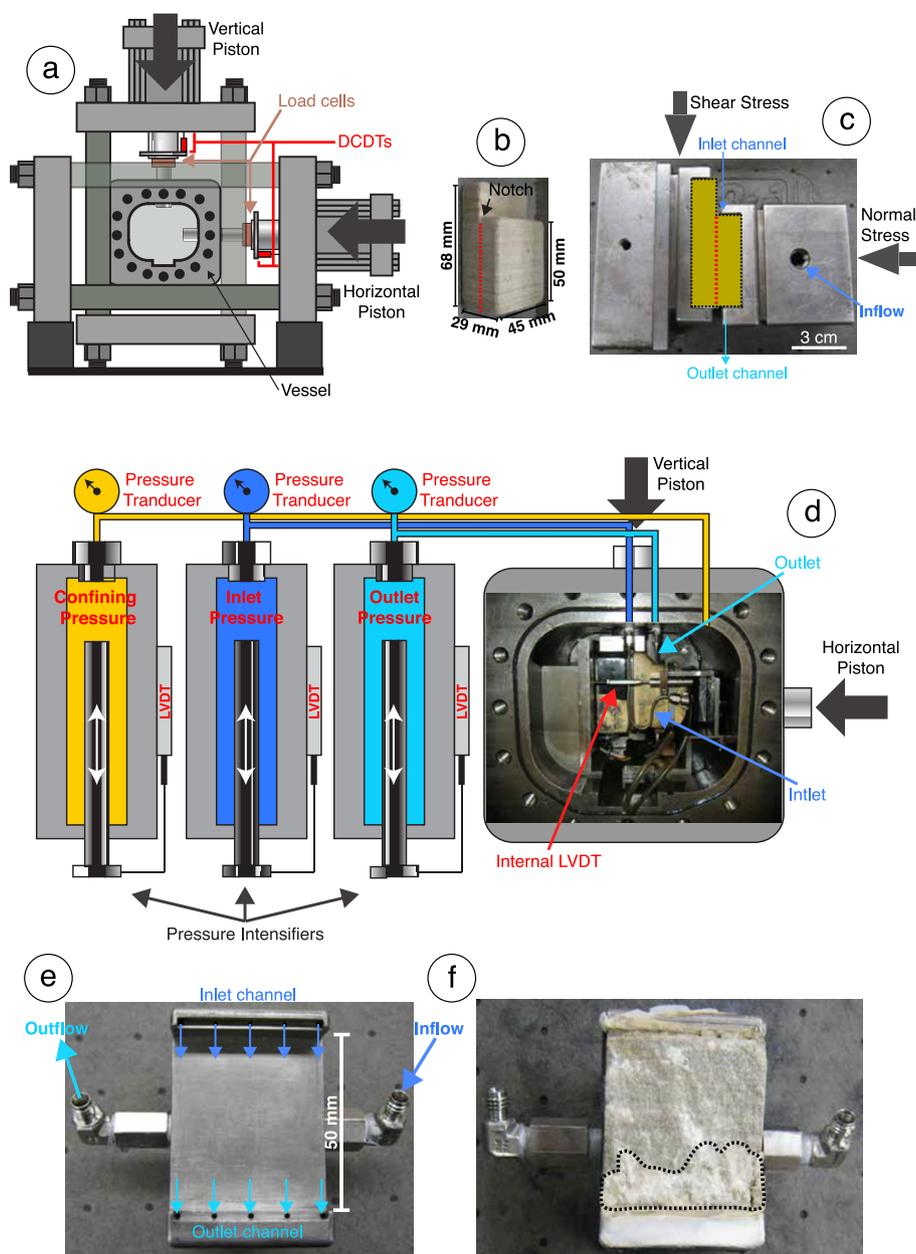
Fig. 1. Detail of the testing machine and experiment configuration. (a) Schematic of the biaxial apparatus showing horizontal and vertical pistons which provide normal and shear stresses on the eventual fracture plane, and pressure vessel. Displacements and stresses of the two pistons are measured with Direct-Current Displacement Transducers (DCDTs) and strain gauge load cells. (b) L-shape sample of Berea Sandstone, showing the eventual fracture plane (red dotted line) that we use to compute the shear stress and the area perpendicular to the flow direction which is used in Darcy's law. (c) Photo of the single direct shear configuration with the two sample holders at both sides of the L-shape sample. As a consequence of the geometry of the configuration, the fracture plane forms vertically (red dotted line) and co-planar with the fluid flow path. (d) Photo of pressure vessel with front door removed showing the sample (within jacket), internal fluid piping, and loading configuration. Fluid lines are connected to servo-controlled intensifiers operated in pressure feedback mode. Linear Variable Differential Transformers (LVDTs) mounted on the intensifier pistons are used to determine flow volumes. An LVDT mounted inside the pressure vessel provides precise measurement of changes in sample thickness during the experiment. (e) Enlargement of one of the sample holders (right side of Fig. 1(c)). Fluid ports and internal conduits in the holders provide fluid flow through the rock sample. (f) Fracture plane after the experiments. The black dotted contour highlights the white gouge particles, which are preferentially located downstream. (For interpretation of the references to color in this figure legend, the reader is referred to the web version of this article.)

Shear load was applied by advancing the vertical piston in servo displacement control at 10 microns/s, which increased stress on the top of the L-shaped block (Fig. 1(a)). Due to the sample geometry and loading conditions, the fracture was constrained to propagate along the long-axis of the specimen – vertically in the loading apparatus (Fig. 1(b), (c)). A thin starter-notch was added at the top of the sample in order to minimize the geometrical complexity of the fracture and to acquire a planar and reproducible fracture geometry for each experiment (Fig. 1(b)). The measured stresses were used to compute shear stress on the

future fracture plane, which had nominal area of 50×45 mm (Fig. 1(b), (c)).

3. Results

After applying the desired triaxial stresses, each experiment proceeded by: (1) applying pore pressure oscillations, simulating dynamic stresses, at one end of intact Berea sandstone samples, (2) fracturing the samples in situ, and (3) resuming pore pressure oscillations post-fracturing. We measured fluid flow under

Table 1
Parameters of the experiments.

Parameters	p3944	p4003	p4022	p4092	p4053	p4054	p4076	p4067	p4079	p4068
Pore fluid	DI[a]	DI	DI	DI	NaCl 25 wt%	NaCl 25 wt%	NaCl 25 wt%	NaCl 5 wt%	NaCl 5 wt%	CaCl$_2$ 5 wt%
	$I \sim 0$[b]	$I \sim 0$	$I \sim 0$	$I \sim 0$	$I = 5.8$	$I = 5.8$	$I = 5.8$	$I = 1$	$I = 1$	$I = 1.4$
	$\mu = 8.9$[c]	$\mu = 8.9$	$\mu = 8.9$	$\mu = 8.9$	$\mu = 16$	$\mu = 16$	$\mu = 16$	$\mu = 9.5$	$\mu = 9.5$	$\mu = 9.5$
Eff. normal stress (MPa)	20	20	19	20	20	20	40	40	20	9.5
Failure shear Stress (MPa)	39	33		37	37	31	59.5		37	25
Residual shear stress (MPa)	22	15		20	16	15.5	39		25	13
Shear offset (mm)	2.1	0.3		1	0.4	0.7	0.5		0.2	1.1
Confining pressure (MPa)	9	9	9	9	9	9	16	16	9	5
Inlet pore pressure (MPa)	3	3	3	3	3	3	3.1	3	3.1	3
Outlet pore pressure (MPa)	2.6	2.8	2.9	2.5	2.8	2.8	2.9	2.8	2.9	2.8
Pore pressure amplitude (MPa)	0.18	0.025	0.01	0.18	0.04	0.06	0.07	0.05	0.04	0.05
	0.3	0.18	0.05	0.5	0.1	0.16	0.19	0.15	0.19	0.17
Log 10(k) [m^2]	−14.9	−14.1	−13.8	−14.6	−14.3	−14.4	−14.6	−14.2	−14.1	−13.9
	−15.1	−14.5		−14.8	−14.4	−14.5	−14.7		−13.9	−13.8
Log 10(Q) [m^3/s]	−7.7	−7.4		−7.3	−8	−7.8	−8.1	−7.5	−7.4	−7.1
	−8	−7.7	−6.8	−7.6	−8.2	−8	−8.2		−7.3	−7

For the permeability and the flow rate, the values at the top represent the measurements before fracturing the samples and the values at the bottom after fracturing.

[a] Deionized water.
[b] Ionic strength (molar/liter).
[c] Fluid viscosity ($\times 10^{-4}$ Pa s), used in Eq. (1).
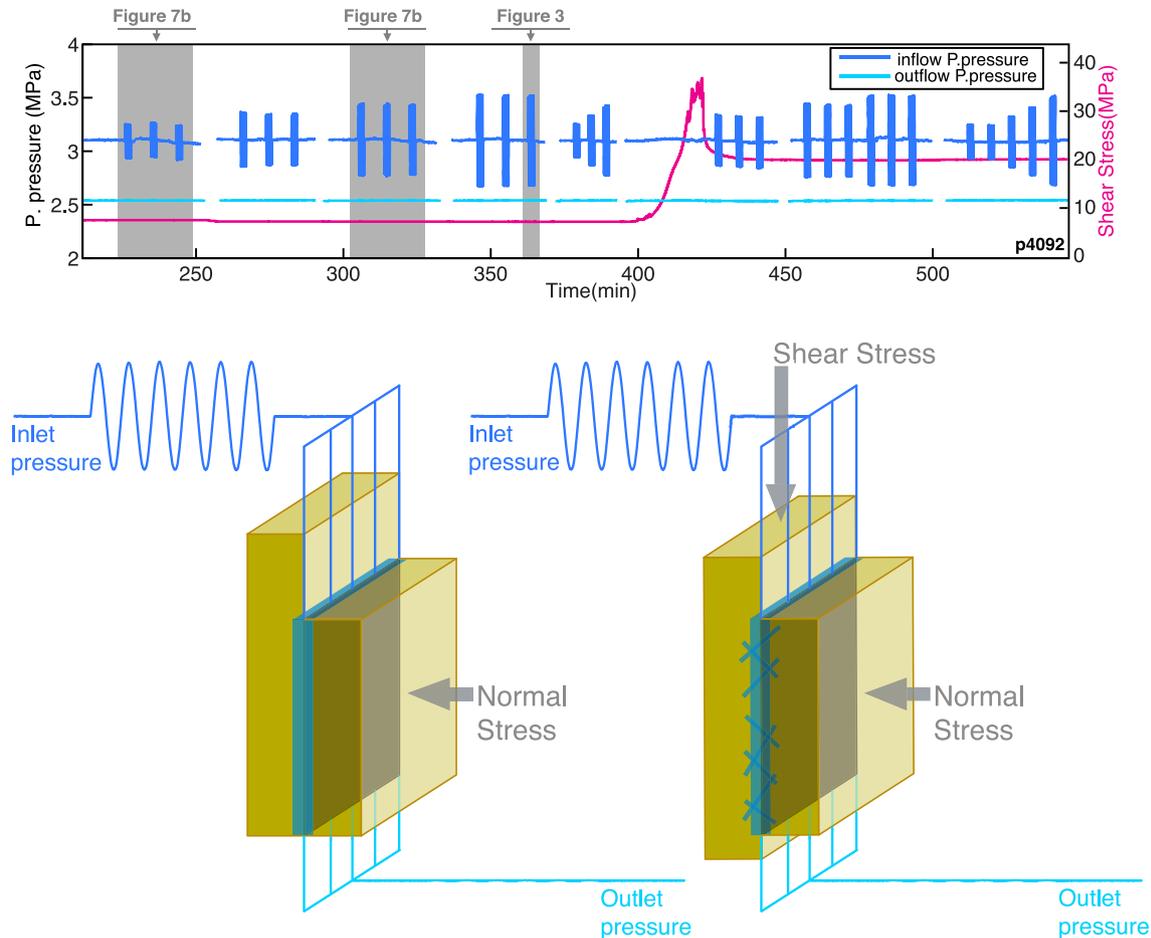
Fig. 2. Experiment overview. (Top) Experimental sequence consists of: (1) applying pore pressure oscillations at the inlet while holding constant the outlet pressure, (2) fracturing in-situ the sample, (3) resuming the dynamic stimulations. (Bottom) Geometry of the fluid flow for the intact and fractured sample. Once the sample fractured, the flow path is co-planar with the fracture plane.

prescribed pore pressure gradients, to derive permeability, and compared sample deformation and permeability for our suite of experiments (Fig. 2).

The full suite of measurements and loading conditions explored were complex. We summarize results of the experiments by providing an overview of each measurement type followed by a detailed description of representative experiments.

3.1. Permeability measurement

We measured inlet and outlet flow volumes to a resolution of 5.1×10^{-5} cm^3 using Linear Variable Differential Transformers (LVDTs) mounted on the pressure intensifier pistons (Fig. 1(d)). The effective permeability k was determined from Darcy's law, by calculating the flow rate over a 2 s window. Flow rates, and perme-

ability, were measured independently at both the inlet and outlet:

$$k = \frac{\mu L}{S} \frac{Q}{\Delta P} \qquad (1)$$

where μ is the fluid viscosity (see Table 1), L is flow path ($\sim$50 mm), S is the cross section of the sample, perpendicular to the flow path ($\sim$45 × 29 mm), and Q is the flow rate.

To determine permeability, we first verified steady state fluid flow by comparing flow rates measured at the inlet and outlet. In the data presented below, we always verified that inlet and outlet flow rate were equal to within $\leqslant$1%. We found two stages where flow rate at the inlet and outlet were not equal: (1) during the pore pressure oscillations (Fig. 3) and (2) when the sample fractured (see additional detail in Appendix A-1). During these two stages, Eq. (1) cannot be applied due to transient storage effects in the sample. For all other times, inlet and outlet flow rates were equal, which implies that the inferred permeability changes discussed below are not due to specific storage effects. Note that this procedure ensures that permeability measurements are made with a precision of $\leqslant$ $\sim$1%.

3.2. Flow and deformation during pore pressure oscillations

Fig. 3 presents detail on pore pressure oscillations from a representative experiment, which followed the overall procedure shown in Fig. 2. We observed the same fundamental response to dynamic stressing before and after samples were fractured. We measured transient deformation of the rock sample normal to the fluid flow direction during pore pressure oscillations using an LVDT mounted directly on the sample (Fig. 1(d)). Fig. 3(a) shows detail of the deformation record, and the corresponding values of strain normal to the flow direction along with the inflow and outflow pore pressure records. Comparison of the three curves illustrates the transient poro-elastic response of the sample. Fluid storage effects are indicated by the phase shift and amplitude damping in flow rate between the inlet, outlet and elastic strain (Fig. 3(a)–(c)). We note that the poro-elastic response of our samples is not connected to any permanent deformation (Fig. 3(a)), which is consistent with the fact that the flow rates for the inlet and outlet track one another after the end of the pore pressure oscillations (Fig. 3(c)).

The steady state flow rates, and hence permeability, differ before and after the application of transient pore pressure oscillations (Fig. 3(c)). Permeability increases transiently and decays back toward the initial value (Fig. 3(d), (e)).

Transient storage in the sample also produces a flow after oscillations. During the pore pressure oscillations, both the transient deformation recorded by the internal LVDT and the difference in flow rates between the inlet and outlet reveal a transient change in the storage (Fig. 3). Thus the release of the fluid trapped within the sample during the oscillatory forcing could mimic the inferred permeability increase. However, in our experiments a comparison of the integrated excess of fluid volume at the inlet and outlet during the pore pressure oscillations indicate that such storage effects are small. The volume of fluid trapped during the oscillatory forcing is at least two orders of magnitudes smaller than the integrated volume of fluid that passed through the sample during 15 min of permeability recovery (Fig. 3). However, to further avoid specific storage effects, we focus our systematic assessment of permeability changes, transient and otherwise, to the period 10 s after the end of the dynamic stimulations, at which time the transient poro-elastic response is clearly negligible (Fig. 3).

3.3. Representative full experimental sequence

We report permeability changes as $(k_1 - k_0)$ where k_0 represents the initial permeability 10 s before oscillations and k_1 the

permeability 10 s after oscillations (Fig. 3(d)). In this way, we ensure that the inlet and outlet flow rates are identical and that our measurements are not biased by storage effects. We find that in most cases pore pressure oscillations produce a direct increase in the flow rate followed by a gradual decay (Fig. 3(c)). In a few cases, we find a decrease in flow rate or no change in flow rate for the lowest range of Pp oscillation amplitude.

Fig. 4(a) presents permeability changes as a function of Pp oscillation amplitude for one representative experiment. For both intact and post-fracture measurements, the dynamic enhancement of permeability is positively correlated with the magnitude of the pore pressure oscillations.

To evaluate the effect of flow on dynamic permeability changes and to compare experiments with different background permeability, we normalized the measured permeability changes by the initial permeability k_0 (Figs. 3(e) and 4(b)). We also normalized the amplitude of the pore pressure oscillations by the background ΔPp values driving flow so that we can compare permeability changes in response to the same relative hydrodynamic forcing across experiments.

Fig. 4(b) presents results of Fig. 4(a) in terms of the normalized permeability and amplitude. A clear positive scaling between both normalized variables is revealed for the intact and fractured cases. For the highest range of the normalized Pp amplitude, the normalized permeability enhancement is slightly higher for fractured samples compared to intact samples.

To simplify discussion below, from this point on we discuss our results in terms of normalized permeability and normalized Pp amplitude, but refer to these quantities as "direct permeability enhancement" and "pore pressure amplitude."

4. Mechanisms of permeability enhancement via dynamic stressing

Our data show: (1) that direct permeability enhancement is positively correlated with the amplitude of the oscillatory forcing and (2) that fractured samples have slightly higher direct permeability enhancement compared to intact samples. We consider three candidate mechanisms for transient permeability enhancement: (i) flow-mobilization of fine particles, (ii) micro-fracture and damage of the solid sample around the main fracture plane followed by healing, and (iii) fracture aperture opening and differential poroelastic behavior of matrix and fractures.

We introduce four distinct tests to evaluate these mechanisms. In all cases we apply pore pressure oscillations in the unfractured or fractured samples and observe permeability changes. To explore the causal mechanisms, we also measure the time histories of elastic strain, compare experiments with varying fluid chemistry, image the rock samples after the experiment, and measure the recovery rate of the permeability to the pre-oscillation level.

4.1. Test 1: Deformation

The first test involves measuring elastic and inelastic deformation of the sample during dynamic stressing. We note that the unclogging mechanism is independent of sample deformation, whereas for microfracture and damage, deformation is expected to accompany permeability enhancement. The pore pressure oscillation and resulting change in effective stress will promote fracture growth and dilation with a magnitude that depends on the fracture density and aperture. For the third mechanism, involving differential poroelastic behavior of fractures and matrix, the mean change in fracture aperture needed to generate a particular permeability change can readily be calculated and should result in observable strain (Appendix A-2).
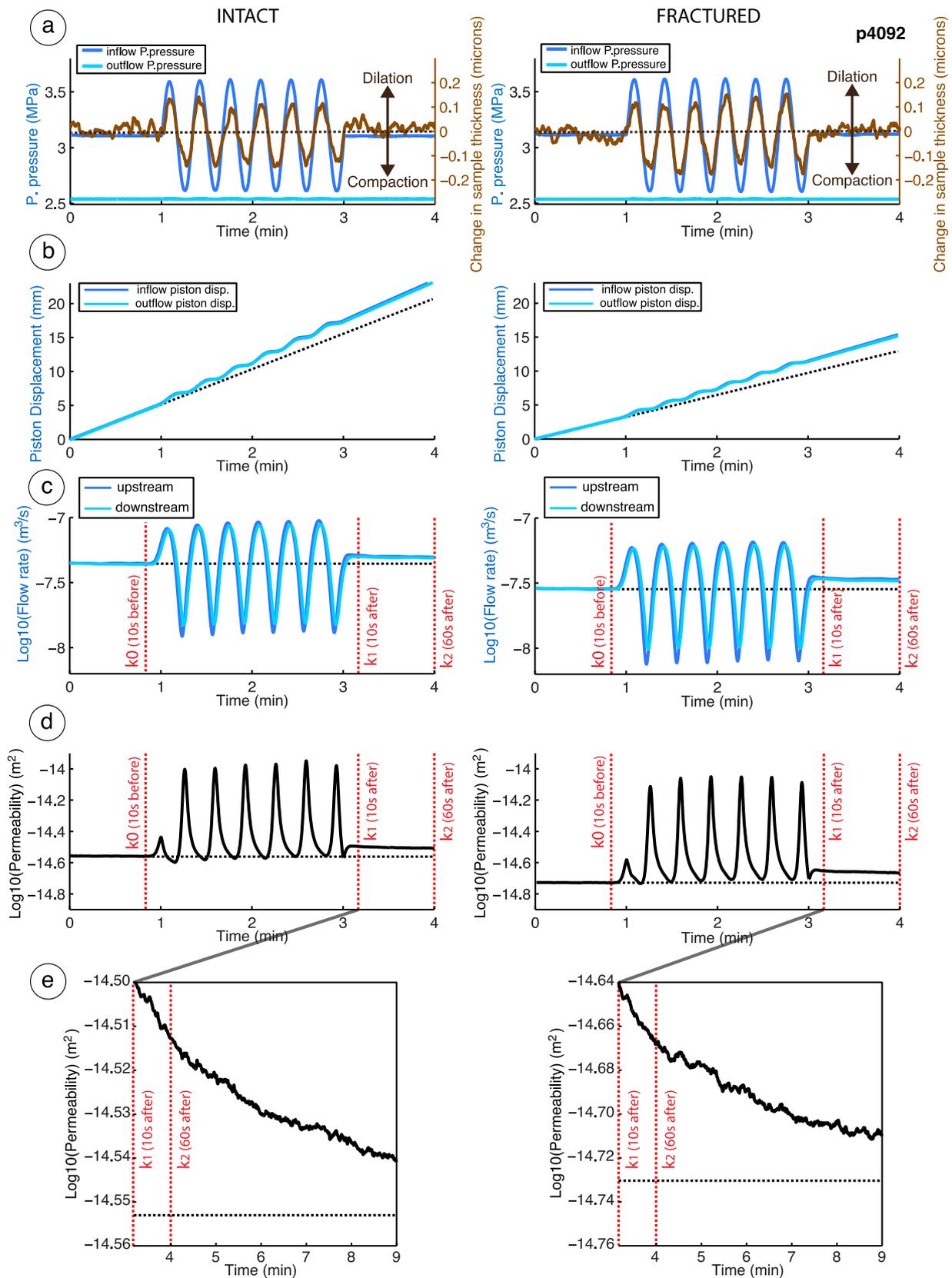
Fig. 3. Detail of dynamic stressing via fluid pressure oscillations for the intact (left column) and fractured sample (right column). (a) Transient changes in sample thickness measured via the internal LVDT during pore pressure oscillations. Dynamic strain amplitude was computed from these displacement measurements. Note that dynamic stressing does not cause permanent deformation of the sample. (b) The P_p piston displacements of the inlet and outlet increase when the oscillations start. The black dotted line shows the piston displacements before the oscillations. The slope is flow rate after accounting for compressibility and specific storage. (c) Note the small time lag and damping attenuation between the maxima of the inlet and outlet flow rates. The increase in flow rates after the pore pressure oscillations is followed by a gradual decay. Notice that before the stimulations and 10 s after, flow rates at the inlet and outlet are identical. (d) and (e) Direct permeability enhancement produced by the pore pressure oscillations followed by its gradual recovery.
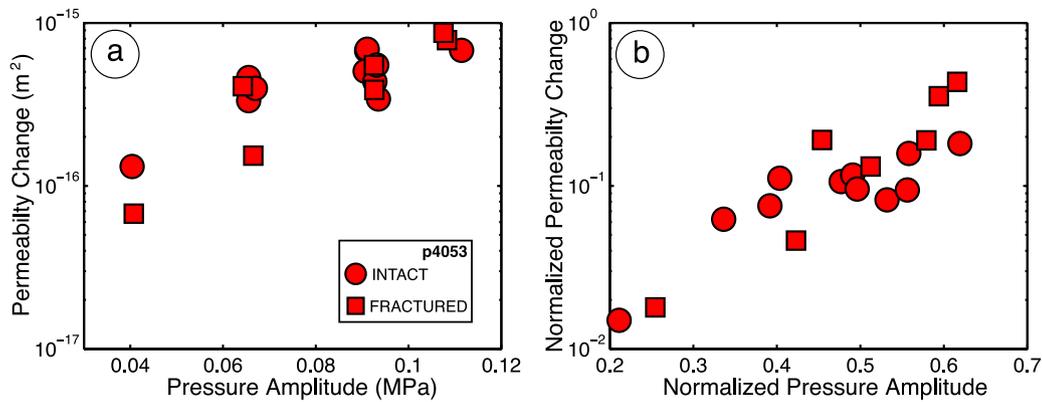
Fig. 4. Permeability increases after the pore pressure oscillations: one representative experiment realized with NaCl 25 wt% as the permeating fluid. For the intact and fractured case, (a) the permeability enhancement ($k_1 - k_0$) and (b) the normalized permeability enhancement ($k_1 - k_0$)/k_0 are positively correlated respectively with (a) the absolute and (b) normalized amplitude of the oscillations. Note the slight higher normalized permeability change at the higher range of pore pressure oscillation amplitude for the fractured sample.

4.2. Test 2: Fluid chemistry

The second test was to adjust the pore fluid chemistry. The susceptibility of the fine particles to be attached or detached to the pore walls should be mainly controlled by the electrostatic interactions between them and the pore-walls (e.g. Khilar et al., 1990; Vaidya and Fogler, 1990; Revil and Glover, 1998; Revil and Leroy, 2004; Ryan and Elimelech, 1996; Rosenbrand et al., 2013). These electrostatic interactions are mainly sensitive to the ionic content (ionic strength and type of ions) of the pore fluid (e.g. Mays, 2007; Tchistiakov, 2000). We used four different pore fluids (deionized water DI, brines with NaCl 25 wt%, NaCl 5 wt%, CaCl$_2$ 5 wt%) in order to span a large spectrum of ionic strength and cation valence (see Table 1). In each case, the brine was made from de-aired DI water. If unclogging is the dominant mechanism, by adjusting the ionic content of the pore fluid, we should induce a difference in the mobility of fine particles, which should produce a difference in the observed dynamic permeability changes. Fluid chemistry is not predicted to have a first-order effect on the other mechanisms.

4.3. Test 3: Sample images

We also examined micro-scale pore textures of rock samples that were not subject to dynamic stressing and compared them to samples with dynamic permeability enhancement. The unclogging mechanism, by flushing out fine particles of the sample, predicts a difference in the fine distribution between these sample sets. Microfracturing predicts a difference in damage. Fracture opening implies a fully elastic behavior of the matrix and therefore predicts no systematic differences in micro-scale texture.

4.4. Test 4: Permeability recovery

A fourth test is the connection of the permeability recovery process to the initial enhancement. Unclogging predicts that the recovery process is dominated by the redistribution of fines and therefore the experiments with the largest permeability increases should have the fastest recovery. Furthermore, water chemistries with highly mobilized fines should have fast recoveries. Micro-cracking should also have a correlation between the recovery and enhancement processes. However, the decoupling of the initial fracture opening and the matrix diffusion process in the third mechanism mandates that the recovery timescale is independent of the amplitude of the initial permeability enhancement.

Note that the comparison of fractured and unfractured behavior does not constitute a powerful test of the mechanism, as all three mechanisms predict an increase in effectiveness of oscillatory pressures to enhance permeability for the fractured case. For the unclogging mechanism, the gouge produced during fracture should increase the availability of fines and therefore the potential for permeability enhancement via mobilization of fines. For the micro-fracturing mechanism, the stress concentrations near the fracture could potentially increase the damage generated by a given oscillatory stress. For the fracture-opening mechanism, the large-scale pre-existing fracture provides a pathway for opening and a locus for slow drainage.

5. Evaluation of tests

5.1. Test 1: Deformation

The measurement of sample deformation, via the internal LVDT (Fig. 1(d)), shows that dynamic stressing does not produce permanent deformation in fractured (Appendix A-2) or intact samples (Fig. 3(a)). For a reasonable model of the deformation and in order to explain the range of permeability enhancement observed, the fracture-opening model suggests an increase of the fracture aperture in a range of 0.25–1 microns (Appendix A-2), which would have been resolvable, but was not observed.

The predicted deformation from microcracking is harder to quantify as there is a trade-off between fracture density and aperture. Unclogging does not predict any deformation.

5.2. Test 2: Fluid chemistry

5.2.1. Intact samples

Prior to fracturing, experiments performed with DI water or a brine with NaCl 25 wt% as permeating fluids generated relatively large permeability enhancements (Fig. 5(a)). For both of these solution chemistries, the observed permeability enhancement at a given forcing amplitude is comparable. In contrast, the intermediate solution chemistries of 5 wt% NaCl and 5 wt% CaCl$_2$ produced much smaller permeability enhancement. The CaCl$_2$ wt% solution was the least effective, with permeability enhancements occurring only for the highest amplitude forcing.

5.2.2. Fractured samples

After fracturing the sample, we found large permeability enhancement for all experiments and solution chemistries (Fig. 5(b)). Even for the CaCl$_2$ 5 wt%, once the sample was fractured, the magnitude of the permeability enhancement was large enough, over the entire experimental range, that we observed a scaling between the amplitude of the oscillatory forcing and permeability enhancement (Fig. 5(b)). As we did not observe any effect of pore fluid
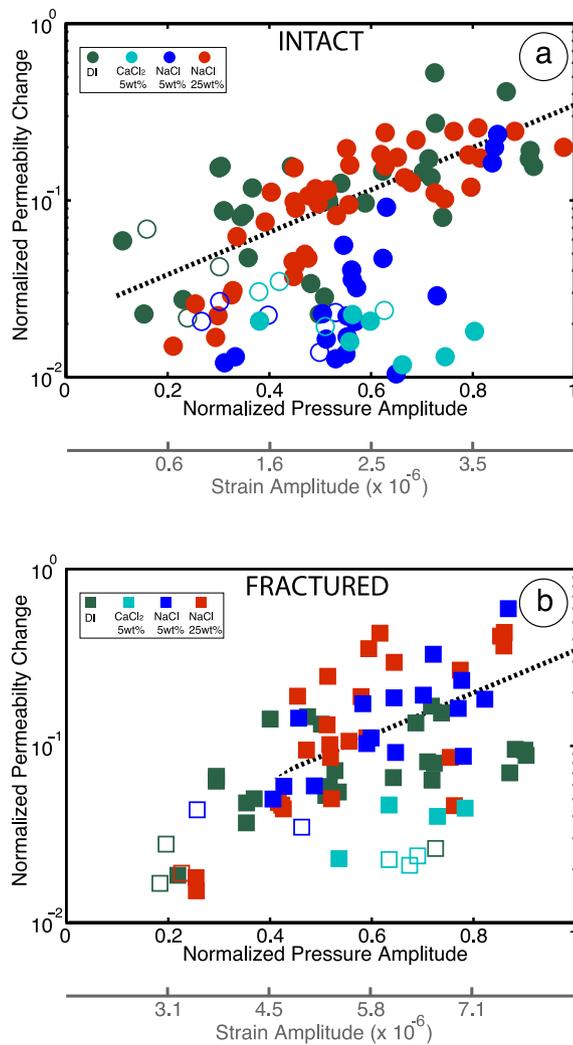
Fig. 5. (a) Permeability changes as a function of the amplitude of pore pressure oscillations: (a) intact and (b) fractured cases. For all fluid chemistries, most of the time, permeability enhancements (filled circle) were observed. Only a few permeability decreases (open circles) were observed for the lowest ranges of the permeability changes and pore pressure oscillation amplitudes. The influence of the permeating fluid chemistry is clearly observed only for the intact case (a). The increase of permeability scales with the amplitude of the stimulations only for DI and NaCl 25 wt%, in contrast to the fractured case (b) where the scaling is observed for all fluid chemistries. To facilitate comparison of the intact and fractured cases, a fiducial line (black dotted) is shown in each panel.

chemistry on permeability enhancement for the fractured case, this test does not rule out any of the three mechanisms.

In modifying the pore fluid chemistry we tune the tendency of fine particles to be attached or detached to the pore walls or between fracture asperities. Ionic strength of the fluid governs the relative adhesion of clay particulates with a minimum in adhesion at intermediate ionic strengths. We will return to a more complete discussion of the physical chemistry of the aqueous solutions in Section 6.1. At this point we simply note that significant coupling between pore fluid chemistry and permeability enhancement is predicted only by the unclogging mechanism. As discussed above, fluid chemistry is not predicted to have a first-order effect on the other two mechanisms.

5.3. Test 3: Sample images

Post-experiment microstructural observations of the fracture surfaces reveal that most of the gouge was distributed in the downstream direction (Fig. 1(f)). In addition, micro-scale textural

analysis of the Berea samples before the experiment reveals that most of the pores are filled by clays (Fig. 6(a)). Scanning Electron Microscope (SEM) observations reveal that these clays are hexagonal plates of kaolinite forming loose aggregates in pore spaces as typically observed for Berea sandstone (e.g. Rosenbrand et al., 2013). In our particular single direct shear configuration, the vertical-preferential flow path was co-planar with the future fracture plane (Fig. 1). Interestingly, after the experiments, the pore throats closer to the preferential flow path appear relatively clean (Fig. 6(b)). In contrast, far from the main flow path, in the bulk of the sample, kaolinite plates are still plugging the pore throats (Fig. 6(c)). These micro-textural observations highlight the role of particle mobilization during our experiments. Gouge powder for the fractured case and kaolinite plates filling the porosity for the intact samples were mobilized and flushed out of the system.

There was no direct evidence of microdamage in the imagery. Fracture opening would have produced no observable difference in the imagery.

5.4. Test 4: Permeability recovery

The rate of the gradual permeability recovery following perturbations can be expressed as $(k_1 - k_2)/k_1$, where k_2 is the permeability 60 s after the end of dynamic stressing (Fig. 3(e)). For a given pore pressure amplitude and for the intact samples, the recovery rate is positively correlated with the direct permeability enhancement immediately following the oscillations (Fig. 7(a)). Consequently, the largest permeability enhancement and therefore the largest recovery rate are observed for the experiments performed with DI water or with NaCl at 25 wt%. These are experiments where fines were easily mobilized due to extreme ionic strengths of the pore fluid (Fig. 7(a)). We posit that the permeability recovery rate is also controlled by the migration of fine particles. After the pore pressure oscillations, fines are more easily entrained by the pore fluid with extreme ionic strengths (DI or NaCl at 25 wt%) and gradually deposited in narrow pore openings/pore throats.

We performed successive pore pressure oscillations with the same amplitude to track the influence of the net fluid flow on permeability enhancement for an equivalent oscillatory forcing (Fig. 2). We found that for the same oscillatory forcing the magnitude of the direct permeability enhancement and its gradual recovery vary inversely with the pore fluid volume flowing through our sample (Fig. 7(b)). For instance, for an experiment using DI water and an intact rock sample, the magnitude of the direct permeability enhancement and the rate of the permeability recovery decreases from the first successive pore pressure oscillation to the last (Fig. 7(b)). The permeability evolution is consistent with unclogging of a finite amount of particulate material. Each time pore pressure oscillations were applied, fine particles were flushed out of the sample. As a result, for the same amplitude of pore pressure oscillations, the magnitude of the direct permeability enhancement and its recovery decreased (Fig. 7(b)). We note that the fluid volume dependence should not necessarily hold in natural aquifers, because the fines should be more available than in our laboratory samples. However, this unanticipated observation is additional evidence that a flow-dependent process, controlled by mobilization of fines, is a suitable mechanism to explain the observed permeability changes.

The healing of microdamage as an explanation for our data is problematic due to the observed fast recovery. During the gradual permeability recovery, we did not detect any long-term deformation between adjacent sets of pore pressure oscillations, as would be expected for either compaction or creep.

Poroelastic recovery following aperture opening should have a consistent recovery rate governed by the matrix properties and in-
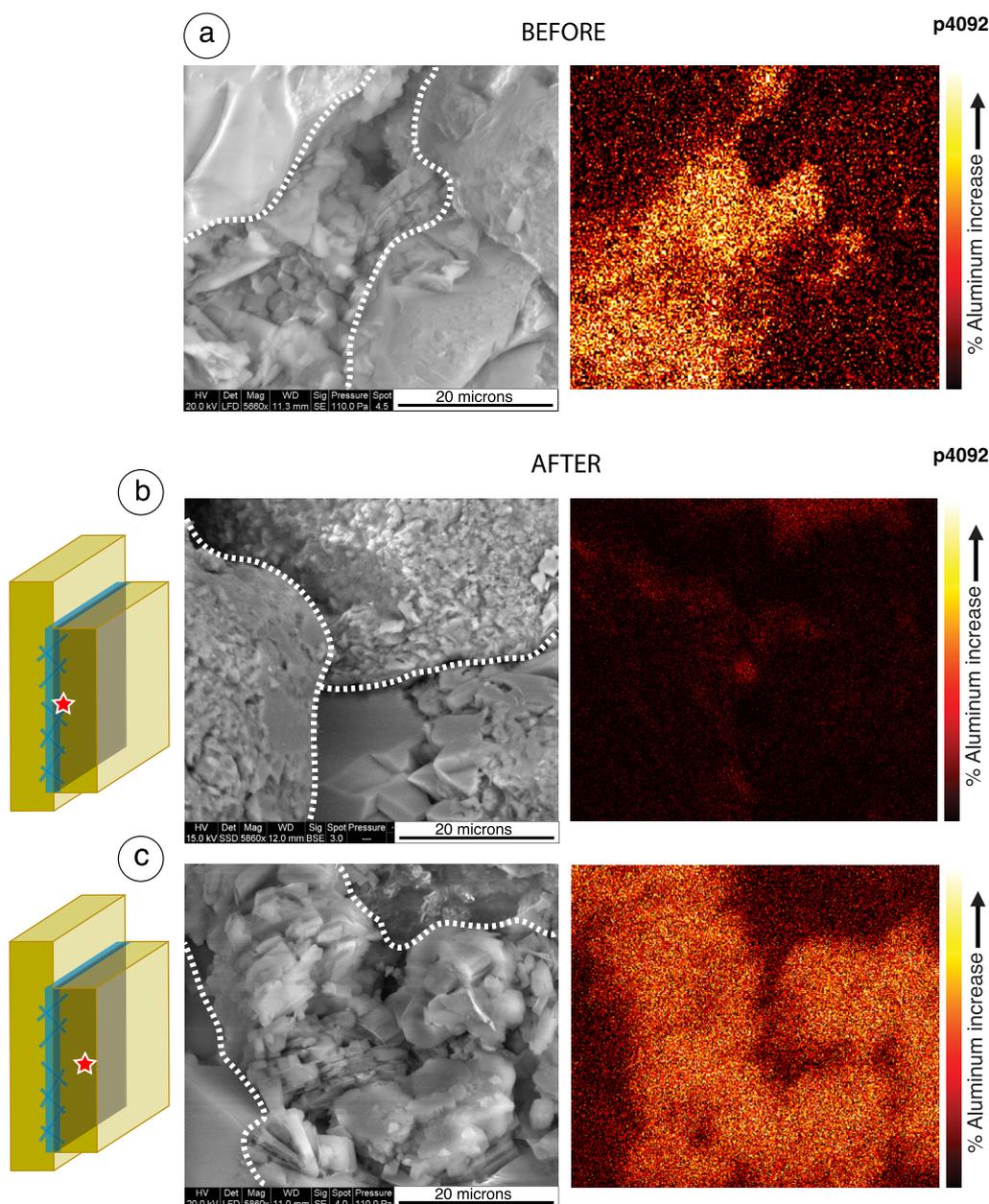
Fig. 6. Micro-textural observation of the pore space before (top) and after (bottom) experiments. All the SEM images (left), and their respective aluminum maps (right), are at the same scale. The white dotted lines emphasize the contours of the quartz grains. (a) In virgin samples, aggregates of hexagonal Kaolinite-plates fill the pore space and EDS (Energy Dispersive Spectroscopy) measurements highlight the presence of abundant aluminum inside the pores further indicating the presence of the clays. After the experiments (c, d), the porosity of the samples close to the vertical preferential flow path appears "clean", without omnipresence of clays plugging the pore throats, and depleted in aluminum (c). As for the sample before the experiment, the pore space inside the bulk of the sample, far from the preferential flow path, appears plugged by aggregates of Kaolinite-plates and enriched in aluminum (d).

dependent of the permeability enhancement. This is not observed (Fig. 7).

6. Fluid chemistry and particle mobilization: Explanations and implications

The balance of the evidence from our four experimental suites favors particle mobilization and unclogging of pore throats as the mechanism for permeability enhancement. Data on: (1) variation of the direct permeability enhancement and its recovery with the fluid chemistry, and (2) visual confirmation of particle mobility are the most direct evidence for unclogging. The lack of deformation during permeability changes argues against either microfracturing or aperture opening as the mechanism. The variability of

the recovery rate is also inconsistent with the aperture opening model.

As the chemical controls on permeability enhancement for intact rocks provide the strongest suite of observations, we now attempt to qualitatively predict the particle mobilization variations from the physical chemistry of the aqueous solutions and then proceed to explore the implications for natural systems.

6.1. Effect of fluid chemistry on mobilization of fines

We varied fluid chemistry to evaluate its affect on mobilization of fine particles. As mentioned previously, we discuss our results in term of normalized permeability change $(k_1 - k_0)/k_0$ and normalized pore pressure amplitude. This allows evaluation of the
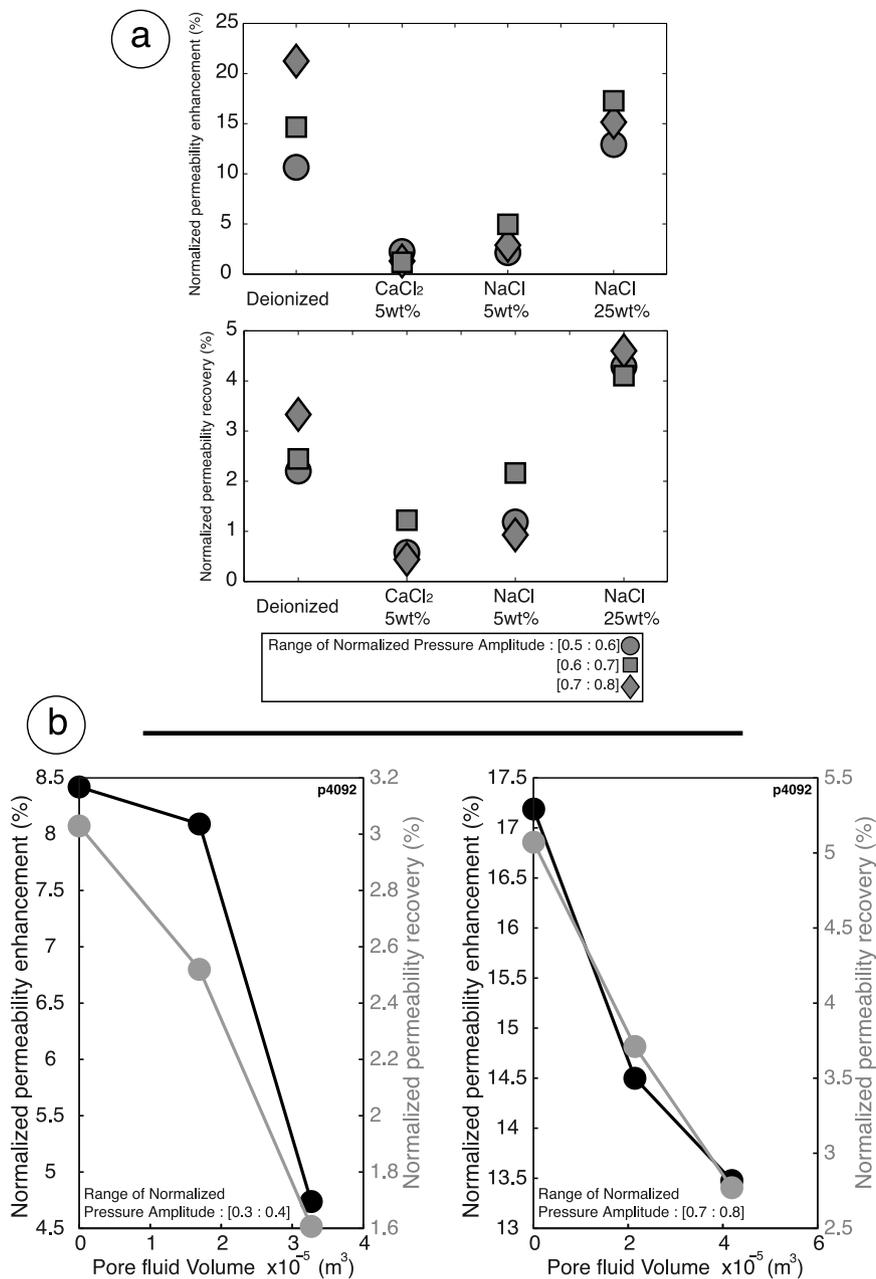
Fig. 7. Co-evolution of direct permeability enhancement $(k_1 - k_0)/k_1$ and its gradual recovery $(k_1 - k_2)/k_1$. (a) Selecting results of averaged direct permeability enhancement and averaged permeability decay after 1 min for three equivalent ranges of oscillatory forcing, we show here that both are correlated. When using DI or NaCl 25 wt% the direct permeability enhancement is higher and its gradual recovery is faster compared to experiments with NaCl 5 wt% or CaCl$_2$ 5 wt%. (b) Comparison of the transient permeability changes for three successive pore pressure oscillations with the same amplitude reveals that both the direct permeability enhancement and the rate of the permeability recovery reduce with the net fluid flow. All results in this figure are for intact cases.

influence of fluid chemistry on particle mobilization, independent of hydrodynamic forcing.

For small particulates in porous media, adhesion and eventual mobilization is governed by the electrical charge at their surfaces. Electrostatic forces between colloidal particles and pore walls dictate detachment and mobilization of such particles. However, attachment and flocculation can also occur when attractive van-der-Waals forces outweigh electrostatic repulsion. In the classical Derjaguin–Landau–Verwey–Overbeek (DLVO) theory, the stability of the colloids is determined by the net force resulting from the competition between the van-der-Waals attraction and the electrostatic repulsion. Temperature, ionic strength, pH, counterion valence can all influence the balance (see Ryan and Elimelech, 1996 for a review). Here, we focus on only the effect of the ionic

strength and counterion valence. No significant dependence on pH was observed in our experiments, which were conducted at constant temperature.

In aqueous solution, commons rock forming minerals usually have negative surface charge (Stumm and Morgan, 1996). The charged surface attracts counterions (here cations, for our pore fluid solutions) for charge balance. While some of the cations remain attached to the surface and form the adsorbed layer, others transit to some distance from the surface and form the diffuse ionic layer. Both the adsorbed and diffuse layers form an electrical double layer.

Deionized water has a low ionic strength and therefore the electrical double layer is thick (Fig. 8). The repulsive potential of the electrostatic interaction extends deep into the aqueous solu-
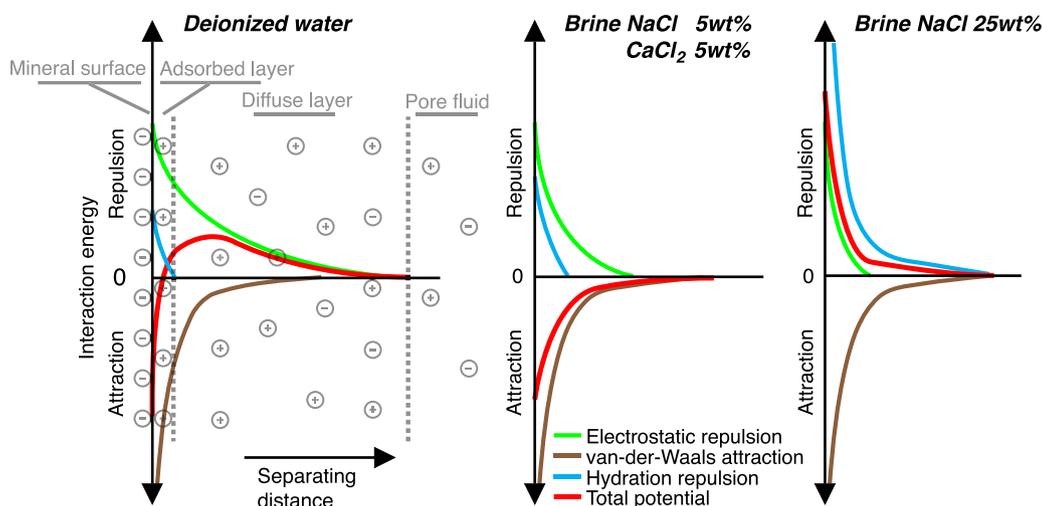
Fig. 8. Illustrations of the evolution of the total potential from the combination of the electrostatic repulsive potential, the van der Waals attractive potential, and the hydration repulsion force. For the DI and brine with NaCl 25 wt%, the total potential was dominated respectively by the electrostatic repulsion and the hydration repulsion. In this case, the fines are easily mobilized. When using either the brine with NaCl 5 wt% or with CaCl₂ 5 wt%, the van-der-Walls attraction dominates and therefore the fines are expected to be stable and attached to the pore-walls.

tion, and is dominant over the van-der-Waals attractive potential. Therefore, fine particles are more easily detached and mobilized from the pore-walls.

When the ionic strength increases, as for our brines with NaCl 5 wt% or CaCl₂ 5 wt%, there are more charges per unit volume of water, so a smaller volume of solution is required to balance the surface charge. Thus, the electrical double layer compresses, and therefore the repulsive potential extends less deeply into the aqueous solution (Fig. 8). However, the van-der-Waals attractive potential does not change with ionic strength, so the resulting total potential is attractive (Fig. 8) and fine particles remain more easily attached to the pore-walls.

At the very high salinity of our brines with NaCl 25 wt%, non-DLVO hydration forces appear to be dominant over the van-der-Waals attractive force (Fig. 8). At high surface charge, and due to the counterion hydration in the compressed double-layer, an extra repulsive force arises because moving the surfaces closer together would require removal of some fraction of the "hydration atmosphere" around these cations (Pashley, 1981). At very high ionic strength, these extra counterion hydration forces prevent adhesive contact, which results in re-peptization and easier mobilization of fines (Fig. 8). Furthermore, the addition of excess salt when using NaCl 25 wt% can cause restabilization of the particles because counterions are adsorbed to such an extent that the particle charge is reversed, causing a repulsion between the particles (Elimelech et al., 1995). In addition, it is important to note here that even though the hypersaline brine NaCl 25 wt% was close to the saturation point, there is no evidence of salt crystals in the effluent fluid.

After fracturing the sample, the influence of fluid chemistry is not significant (Fig. 5(b)). The fracture process probably produces sufficient fine particles (i.e. gouge) that even for strongly adhesive chemistries (NaCl 5 wt% or CaCl₂ 5 wt%) fines are available to be mobilized during the pore pressure oscillations. This effect could explain higher efficiency of the pore pressure oscillations for mobilization of fines and therefore greater permeability enhancement for fractured-compared to intact samples.

Although the above analysis provides a qualitative understanding of the stability of fine particles, it is beyond the scope of our work to quantitatively describe the way fluid chemistry influences the degree of fine particle mobilization. Our goal was to evaluate the evidence for the major candidate mechanisms for permeability enhancement. We have shown that by changing the fluid chem-

istry it was possible to modify the degree of permeability enhancement, which favors mobilization of fine particles as a mechanism in our experiments.

6.2. Implications for field observations

Our experiments favor a flow-dependent process related to the mobilization of fines activated by dynamic shaking as the origin of changes in local permeability (Manga et al., 2003; Manga and Brodsky, 2006; Elkhoury et al., 2006; Doan et al., 2007; Xue et al., 2013). Our range of direct permeability enhancement and dynamic strain amplitude (inferred from the actual deformation of our samples) is consistent with natural observations (Manga et al., 2012), that are respectively 1–60% and 7×10^{-7} to 7×10^{-6} (Fig. 8). However, the applied pressure gradients in the experiments exceed those in nature.

The recovery rate observed in our experiments is faster than that observed in natural cases. The time to recover the initial permeability is about half an hour for the largest pore pressure oscillations with the strongest permeability enhancement (60%). In contrast, in nature the characteristic time for the permeability recovery is often of the order of months (Elkhoury et al., 2006; Manga et al., 2012). Our results show that the recovery rate is dependent on the pore fluid chemistry and the flow rate. In the absence of fluid chemistry changes, the rate of pore throat re-clogging by fine particles is dependent on the interstitial fluid velocity. The flow rates of natural aquifers are significantly slower than in our experiments. The difference of fluid velocity could explain the difference of recovery rate of our experiments with that in nature.

As demonstrated in our experiments, injection of certain chemistry fluids favors fines mobilization and consequently permeability increase. Regions where pore fluids change suddenly may experience stronger permeability enhancement, and therefore facilitate the diffusion of pore fluid pressure. We speculate that this feature of dynamic permeability enhancement could have a connection to some of the key features of dynamic earthquake triggering.

Earthquake-triggering by seismic waves is sometimes explained by the fact that small dynamic strains could be sufficient to destabilize critically loaded faults by increasing the pore pressure (e.g. Brodsky and Prejean, 2005). Dynamic permeability enhancement is one mechanism-candidate to explain earthquake-triggering by seismic waves (Brodsky et al., 2003; van der Elst et al., 2013). In
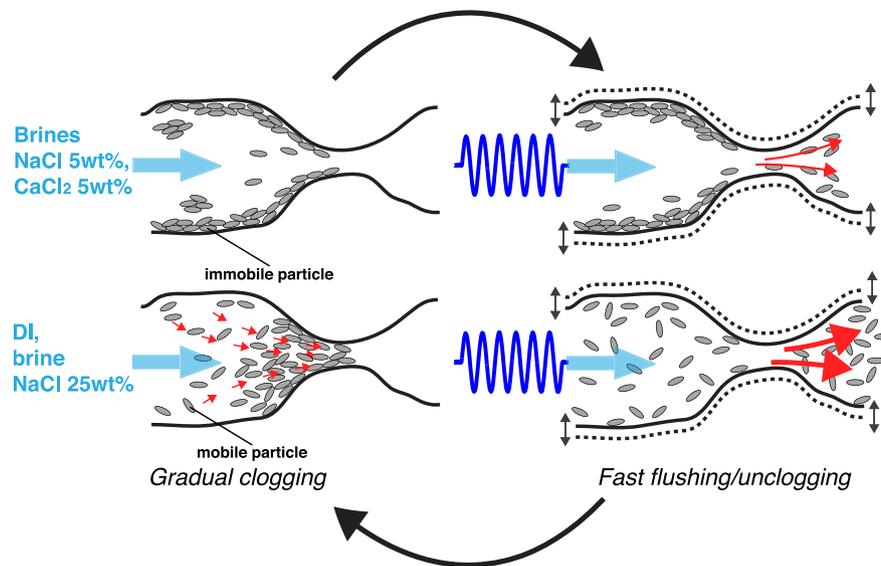
Fig. 9. Cartoon of the unclogging and re-clogging process. Between two sets of pore pressure oscillations, the fine particles migrate gradually to the pore throats (or between fracture asperities), explaining the long-term permeability recovery. During the oscillations, the fines initially plugged in the pore throats (or between fracture asperities) are flushed, producing the direct permeability enhancement observed in our experiments. Fluid chemistry controls fines mobilization during both flushing and the ensuing gradual migration. When using a pore fluid with an intermediate ionic strength (a brine with NaCl 5 wt% or CaCl$_2$ 5 wt%), that is in natural aquifers a fluid that reached an equilibrium with the surrounding rock, fines are more strongly attached to the pore walls and are less easily mobilized. Injection of unusual chemistry fluids with extreme ionic strengths (DI or brine with NaCl 25 wt%) favor mobility of fines, which explains the higher direct permeability enhancements and recovery rates in these cases.

this scenario, unclogging of fine particles by dynamic stress will increase the aquifer permeability and accelerate diffusion of pore pressure into faults.

Certain areas are most susceptible to dynamic triggering than others. Volcanic, hydrothermal and deep wastewater injection sites are all among the most triggerable regions (Hill et al., 1993; Brodsky and Prejean, 2005; Husen et al., 2004; van der Elst and Brodsky, 2010; van der Elst et al., 2013). In all of these cases, the pore fluid chemistry should be more variable than in regions where longer residence times allow fluid to reach equilibrium with the surrounding rock. As demonstrated in our experiments, injection of unusual chemistry fluids favors the mobilization of fines and consequently permeability increase. Regions where pore fluids change may experience stronger permeability enhancement, and therefore may be prone to the resultant pore fluid pressure changes and dynamic earthquake-triggering.

In addition, in areas of deep waste water injections, a long delay is observed between the start of injection and the onset of dynamically triggered earthquakes (van der Elst et al., 2013). This delay could be related to the characteristic time between the onset of the mobilization of the fines, by injection of unusual fluids, and their settling into clogged positions in pore throats. Dynamic stressing by seismic waves that occurs before pore throats are clogged will have no effect on permeability and therefore these waves will be less likely to trigger earthquakes than waves that arrive after pore throats are clogged.

7. Conclusions

By using an experimental procedure designed to track both the hydrological and mechanical response to dynamic stresses via pore pressure oscillation, we have shown that a flow-dependent process is the most suitable candidate to explain observed dynamic permeability changes in Earth's crust. Our experimental results demonstrate that permeability enhancement via dynamic stressing does not require permanent deformation. Therefore the dynamic permeability enhancement we observe is not easily explained by micro-cracking or differential fracture compliance effects. Microscopic observations and fluid chemistry coupling give positive evi-

dence of fines mobilization. Both the direct permeability enhancement and its slow recovery are best explained by the fast flushing and gradual re-clogging of the fines at the pore throats or between fracture asperities (see Fig. 9). Our results imply that regions and times with unusual fluid chemistries should be particularly sensitive to dynamic permeability enhancement. Wastewater injection sites, geothermal fields and fault zones flushed with fluid fluxes following an earthquake are all reasonable candidates for future field studies.

Appendix A. Supplementary material

Supplementary material related to this article can be found online at http://dx.doi.org/10.1016/j.epsl.2014.02.025.

References

Beresnev, I.A., Johnson, P.A., 1994. Elastic-wave stimulation of oil production: A review of methods and results. Geophysics 59, 1000–1017. http://dx.doi.org/10.1190/1.1443645.

Brodsky, E.E., Prejean, S.G., 2005. New constraints on mechanisms of remotely triggered seismicity at Long Valley Caldera. J. Geophys. Res. 110, B04302. http://dx.doi.org/10.1029/2004JB003211.

Brodsky, E.E., Roeloffs, E., Woodcock, D., Gall, I., Manga, M., 2003. A mechanism for sustained groundwater pressure changes induced by distant earthquakes. J. Geophys. Res. 108 (B8), 2390. http://dx.doi.org/10.1029/2002JB002321.

Coble, R.W., 1965. The effects of the Alaskan earthquake of March 27, 1964, on ground water in Iowa. Proc. Iowa Acad. Sci. 72, 323–332.

Doan, M., Brodsky, E.E., Agnew, D.C., 2007. Mechanisms of permeability enhancement by seismic waves at Piñon flat observatory. Eos Trans. AGU 88 (52), 0481. Fall Meet. Suppl., Abstract H11B.

Elimelech, M., Gregory, J., Jia, X., Williams, R.A., 1995. Particle Deposition and Aggregation – Measurement, Modelling and Simulation. Butterworth-Heinemann, Elsevier, p. 62.

Elkhoury, J.E., Brodsky, E.E., Agnew, D.C., 2006. Seismic waves increase permeability. Nature 441, 1135–1138. http://dx.doi.org/10.1038/nature04798.

Elkhoury, J.E., Niemeijer, A., Brodsky, E.E., Marone, C., 2011. Laboratory observations of permeability enhancement by fluid pressure oscillation of in-situ fractured rock. J. Geophys. Res. 116, B02311. http://dx.doi.org/10.1029/2010JB007759.

Faoro, I., Elsworth, D., Marone, C., 2012. Permeability evolution during dynamic stressing of dual permeability media. J. Geophys. Res. 117, B01310. http://dx.doi.org/10.1029/2011JB008635.

Gangi, A.F., 1978. Variation of whole and fractured porous rock permeability with confining pressure. Int. J. Rock Mech. Min. Sci. Geomech. Abstr. 15, 249–257.

Hill, D.P., et al., 1993. Seismicity remotely triggered by the magnitude 7.3 Landers, California, earthquake. Science 260 (5114), 1617–1623. http://dx.doi.org/10.1126/science.260.5114.1617.

Husen, S., Taylor, R., Smith, R.B., Heasler, H., 2004. Changes in geyser eruption behavior and remotely triggered seismicity in Yellowstone National Park produced by the 2002 M 7.9 Denali fault earthquake, Alaska. Geology 32 (6), 537–540. http://dx.doi.org/10.1130/G20381.1.

Ikari, M., Saffer, D.M., Marone, C., 2009. Frictional and hydrologic properties of clay-rich fault gouge. J. Geophys. Res. 114, B05409. http://dx.doi.org/10.1029/2008JB006089.

Khilar, K.C., Vaidya, R.N., Fogler, H.S., 1990. Colloidally-induced fines release in porous media. J. Pet. Sci. Eng. 4, 213–221.

Kouznetsov, O.L., Simkin, E.M., Chilingar, G.V., 1998. Improved oil recovery by application of vibro-energy to waterflooded sandstone. J. Pet. Sci. Eng. 19 (191), 200. http://dx.doi.org/10.1016/S0920-4105(97)00022-3.

Liu, W., Manga, M., 2009. Changes in permeability caused by dynamic stresses in fractured sandstone. Geophys. Res. Lett. 36, L20307. http://dx.doi.org/10.1029/2009GL039852.

Manga, M., 2007. Did an earthquake trigger the may 2006 eruption of the Lusi mud volcano?. Eos 88, 201.

Manga, M., Brodsky, E.E., 2006. Seismic triggering of eruptions in the far field: Volcanoes and geysers. Annu. Rev. Earth Planet. Sci. 34, 263–291. http://dx.doi.org/10.1146/annurev.earth.34.031405.125125.

Manga, M., Rowland, J.C., 2009. Response of Alum Rock springs to the October 30, 2007 Alum Rock earthquake and implications for the origin of increased discharge after earthquakes. Geofluids 9, 237–250. http://dx.doi.org/10.1111/j.1468-8123.2009.00250.x.

Manga, M., Wang, C.Y., 2007. Earthquake hydrology. In: Kanamori, H. (Ed.), Treatise on Geophysics. In: Earthquake Seismology, vol. 4. Elsevier, Boston, Mass, pp. 293–320.

Manga, M., Brodsky, E.E., Boone, M., 2003. Response of stream flow to multiple earthquakes. Geophys. Res. Lett. 30 (5), 1214. http://dx.doi.org/10.1029/2002GL016618.

Manga, M., Beresnev, I., Brodsky, E.E., Elkhoury, J.E., Elsworth, D., Ingebritsen, S.E., Mays, D.C., Wang, C.-Y., 2012. Changes in permeability caused by transient stresses: Field observations, experiments, and mechanisms. Rev. Geophys. 50, RG2004. http://dx.doi.org/10.1029/2011RG000382.

Mays, D.C., 2007. Using the Quirk–Schofield diagram to explain environmental colloid dispersion phenomena. J. Nat. Resour. Life Sci. Educ. 36, 45–52.

Nikolaevskiy, V.N., Lopukhov, G.P., Liao, Y., Economides, M.J., 1996. Residual oil reservoir recovery with seismic vibrations. SPE Prod. Facil. 11, 89–94. http://dx.doi.org/10.2118/29155-PA.

Pashley, R.M., 1981. Hydration forces between mica surfaces in aqueous electrolyte solutions. J. Colloid Interface Sci. 80 (I).

Revil, A., Glover, P.W.J., 1998. Nature of surface electrical conductivity in natural sands, sandstones, and clays. Geophys. Res. Lett. 25 (5), 691–694.

Revil, A., Leroy, P., 2004. Constitutive equations for ionic transport in porous shales. J. Geophys. Res. 109 (B03208). http://dx.doi.org/10.1029/2003JB002755.

Roberts, P.M., 2005. Laboratory observations of altered porous fluid flow behavior in Berea sandstone induced by low-frequency dynamic stress stimulation. Acoust. Phys. 51, 140–148. http://dx.doi.org/10.1134/1.2133962.

Roberts, P.M., Abdel-Fattah, A.I., 2009. Seismic stress stimulation mobilizes colloids trapped in a porous rock. Earth Planet. Sci. Lett. 284, 538–543. http://dx.doi.org/10.1016/j.epsl.2009.05.017.

Roberts, P.M., Esipov, I.B., Majer, E.L., 2003. Elastic wave stimulation of oil reservoirs: Promising EOR technology?. Lead. Edge 22, 448–453. http://dx.doi.org/10.1190/1.1579578.

Roeloffs, E.A., 1998. Persistent water level changes in a well near Parkfield, California, due to local and distant earthquakes. J. Geophys. Res. 103, 869–889. http://dx.doi.org/10.1029/97JB02335.

Rosenbrand, E., Fabricius, I.L., Kets, F., 2013. Kaolinite mobilization in sandstone: pore plugging vs suspended particles. In: Proceedings, Thirty-Eighth Workshop on Geothermal Reservoir Engineering. Stanford University. SGP-TR-198.

Ryan, J.N., Elimelech, M., 1996. Colloid mobilization and transport in groundwater. Colloids Surf. A, Physicochem. Eng. Asp. 107, 1–56.

Samuelson, J., Elsworth, D., Marone, C., 2009. Shear-induced dilatancy of fluid saturated faults: Experiment and theory. J. Geophys. Res. 114, B12404. http://dx.doi.org/10.1029/2008JB006273.

Stumm, W., Morgan, J.J., 1996. Aquatic Chemistry, 3rd ed. Wiley–Interscience, New York.

Tchistiakov, A.A., 2000. Physico-chemical aspects of clay migration and injectivity decrease of geothermal clastic reservoirs. In: Proceedings World Geothermal Congress 2000 Kyushu – Tohoku.

Thomas, J.M., Chrysikopoulos, C.V., 2007. Experimental investigation of acoustically enhanced colloid transport in water-saturated packed columns. J. Colloid Interface Sci. 308, 200–207.

Vaidya, R.N., Fogler, H.S., 1990. Formation damage due to colloidally induced fines migration. Colloids Surf. 50, 215–229.

van der Elst, N., Brodsky, E.E., 2010. Connecting near-field and far-field earthquake triggering to dynamic strain. J. Geophys. Res. 115, B07311. http://dx.doi.org/10.1029/2009JB006681.

van der Elst, N.J., Savage, H.M., Keranen, K.M., Abers, G.A., 2013. Enhanced remote earthquake triggering at fluid-injection sites in the midwestern United States. Science 341, 164–167. http://dx.doi.org/10.1126/science.1238948.

Xue, L., et al., 2013. Continuous permeability measurements record healing inside the Wenchuan earthquake fault zone. Science 340, 1555–1559. http://dx.doi.org/10.1126/science.1237237.